Damage and helium migration induced in fluorapatite sinters by swift heavy ion irradiations

S. Miro [a,*], J.M. Costantini [b], J. Haussy [c], D. Chateigner [d], E. Balanzat [e]

[a] CEA, DEN, Service de Recherches de Métallurgie Physique, Laboratoire JANNUS, F-91191 Gif-sur-Yvette, France
[b] CEA, DEN, SRMA, F-91191 Gif-sur-Yvette, France
[c] CEA, DAM, DIF, F-91297 Arpajon, France
[d] CRISMAT (CNRS UMR 6508), ENSICAEN, IUT-Caen, Université de Caen Basse-Normandie, 6 Bd du Maréchal Juin, 14050 Caen Cedex, France
[e] CIMAP, Boulevard H. Becquerel, BP 55027, 14076 Caen Cedex 05, France

ARTICLE INFO

ABSTRACT

We have studied the damage induced in fluorapatite ($Ca_{10}(PO_4)_6F_2$) sinters after 70-MeV Kr, 120 MeV I and 163-MeV Au ion irradiations at room temperature. On the basis of X-ray powder diffraction data we conclude that fluorapatite is not completely amorphized due to ion-induced recrystallization. This recrystallization of the amorphous phase is greatly enhanced for Au ions with a high electronic stopping power. We also have used the $^3He(d, p)$ ^4He nuclear reaction to study the migration of implanted 3-MeV ^3He ions after swift heavy ion irradiations. The proton yield curves versus deuteron energy for irradiated samples exhibit two bumps for high fluences. These excitation curves are deconvoluted by using a computer code based on a two-diffusion equation model of helium atoms in two accumulation zones. Optimizations of the model parameters give access to the diffusion coefficients and helium depth profiles in the two zones. This yields two broad peaks in the helium depth profiles, the first one is near the end-of-range region and the second one is shifted at about half way between the surface and the first peak. This shift is interpreted as a Radiation-Enhanced Diffusion (RED) effect which is found to increase with fluence for Kr ions, and with electronic stopping power from Kr to Au ions.

© 2012 Published by Elsevier B.V.

1. Introduction

Among the various matrices (apatite, monazite, hollandite, zirconolite, iodosodalite, titanite) investigated for nuclear waste storage purposes, apatites were considered long ago since their structure allows to incorporate many radionuclides like trivalent minor actinides (Am^{3+}, Cm^{3+}) and fission products (I^-, Cs^+) of ^{235}U. Apatite, in its most common high-symmetry representation, [1] is the generic name of a family of chemical formula $Me_{10}(XO_4)_6A_2$ which crystallize in the hexagonal system with space group $P6_3/m$ [1]. The Me atoms (Ca^{2+}, Ba^{2+}, etc.) and the XO_4 group (PO_4^{3-}, VO_4^{3-}, etc.) stand for divalent cations and trivalent anions respectively. The charge is balanced by monovalent anions A (F^-, I^-, etc.).

During storage, the helium content generated in matrices by α-emitters could reach large values (>1 at.%) [2]. Since the solution energy of helium in solids is generally large, [3] helium atoms will tend to coalesce and form bubbles inducing detrimental modifications of the material's structure and mechanical properties (e.g. embrittlement) [4]. Radiation damage may either inhibit or enhance helium diffusion, depending on the type of defects that are produced [5]. Actually, point defects induced by alpha recoils can trap helium atoms whereas extended ones may promote pipe diffusion. It is thus of utmost importance to understand helium thermal diffusion, but also the Radiation-Enhanced Diffusion (RED) of helium induced by ion bombardment, in relation to the radiation damage.

In our previous studies, we showed the influence of the chemical composition on the helium thermal diffusion process [6] and on the RED effect induced by swift Au ion irradiation, [7] by using Nuclear Reaction Analysis (NRA). During a thermal diffusion process, [6] diffusion is easier in a completely silicated apatite $Ca_4Nd_6(SiO_4)_6F_2$ than in a completely phosphated apatite $Ca_{10}(PO_4)_6F_2$, i.e., when the tunnel size increases. No significant difference was found between single crystals and sintered samples of the completely phosphated apatite. On the contrary, during the RED effect, [7] diffusion is enhanced when the damage created by irradiation is larger, i.e. in $Ca_{10}(PO_4)_6F_2$ rather than in $Ca_4Nd_6(SiO_4)_6F_2$ [6]. We have also previously found that amorphous tracks are produced by swift heavy ion irradiations, but no complete amorphization is achieved [8,9].

The purpose of the present paper is to study the damage and the RED effect induced by heavy ion irradiation in the fluorapatite ($Ca_{10}(PO_4)_6F_2$) in relation to the material's modifications.

* Corresponding author. Tel.: +33 1 69 08 86 13; fax: +33 1 69 08 68 67.
E-mail address: sandrine.miro@cea.fr (S. Miro).

Moreover, we give details of the diffusion model, developed to take into account the RED effect which was briefly sketched in a previous paper [7].

2. Experiments

The $Ca_{10}(PO_4)_6F_2$ ceramics were synthesized by a reactive sintering of precursors CaF_2, CaO and $Ca_2P_2O_7$ in stoichiometric amounts. After being crushed, precursors were compacted in a pellet (diameter of 11 mm and thickness of 1 mm) by pressing at 200 MPa. A heat treatment was thus applied at 1500 °C during 6 h under nitrogen flow [6–10]. Acicular grains are formed in these sinters with sizes about $5 \times 100 \ \mu m^2$. Implantations at room temperature (RT) with 3-MeV ^3He ions at a fluence of $10^{16} \ cm^{-2}$ were carried out at the Van de Graaff accelerator of the InESS Laboratory (Strasbourg). The projected range (R_p) and longitudinal straggling (ΔR_p) of ^3He ions calculated with the SRIM2010 code [11] are respectively 10.40 μm and 0.23 μm (Table 1). Helium peak concentrations were estimated to about 0.26 at.% ($1.85 \times 10^{20} \ cm^{-3}$) by using SRIM2010 data [11] (Table 1). Samples were subsequently irradiated at RT with 70-MeV Kr ions (at fluences of $10^{12} \ cm^{-2}$ and $10^{13} \ cm^{-2}$) at the IRRSUD beam line of the GANIL facility (Caen), or with 163-MeV Au ions (at a fluence of $10^{12} \ cm^{-2}$) at the VIVITRON facility (Strasbourg). Low ion fluxes were used ($\varphi \sim 10^8 \ cm^{-2} \ s^{-1}$) in order to prevent beam-induced sample heating. All SRIM2010-code parameters for the He ion implantation and heavy ion irradiations are displayed in Table 1.

The ^3He depth profiles were determined by NRA with the $^3He(d, p)^4He$ reaction using the milli-probe of Van de Graaff accelerator at the INSTN (CEA, Saclay) using a deuteron beam with a diameter of 0.5 mm at an incidence angle of 0°. For a given deuteron energy, emitted protons were recorded with a surface barrier detector at an angle of 150°. The detector solid angle and energy resolution were 2.35 mSr and 17 keV, respectively, and was masked with a 29 μm mylar foil to stop the backscattered deuterons. The broad 'resonance' cross-section of this nuclear reaction is not adequate to obtain a good depth resolution for the ^3He depth profile [6]. Our solution was to sweep the deuteron beam energy gradually from 0.3 to 1.8 MeV, in order to shift the maximum of the cross-section inside the material. The proton yield is plotted on an excitation curve versus deuteron energy (Fig. 1) which is a convolution of the ^3He depth profile with the cross-section. Thus, helium depth profiles can be extracted from the excitation curves of the as-implanted and annealed samples.

The computer code, used to extract the helium depth profiles, is a new version of the (AGEING) computer code, developed to take into account of the RED effect, observed upon Au ion irradiation in a previous paper [7]. The first version of this computer code was successfully used to study the thermal diffusion of ^3He in fluorapatites [6,8,12] and zirconia [13].

X-ray diffraction (XRD) was operated on a four-circle diffractometer equipped with a curved position sensitive detector (INEL CPS 120), using the Copper Kα radiation, [14] directly on the ceramics. The use of the CPS enables the acquisition of the full diagram within $0° \leqslant 2\theta \leqslant 120°$ range in a single step. The incidence

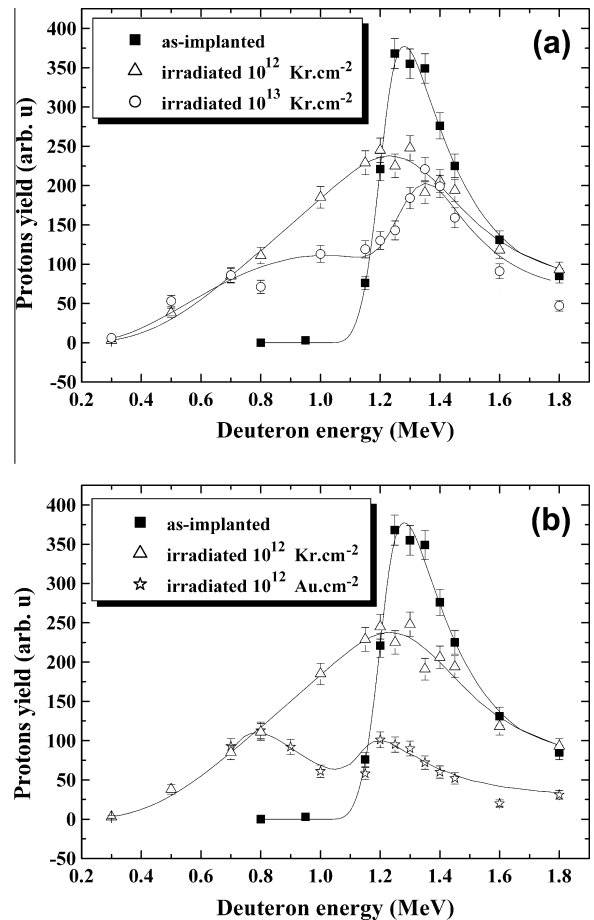**Fig. 1.** Experimental and simulated excitation curves obtained with the $^3He(d, p)^4He$ nuclear reaction: at different fluences for Kr ion irradiation (a), and different electronic stopping powers for Kr and Au ion irradiations at the same fluence ($10^{12} \ cm^{-2}$) (b).

angle of the X-ray beam was 5° relative to the sample plane in order to probe the near surface of the sintered pellets. Under this condition, 97% of the diffracted signal comes from the first 9 μm of the sample, which is smaller than the ion projected ranges (Table 1), ensuring that X-ray information only comes from the ion-irradiated depth. Collimating slits of 200 μm were used in order to decrease as much as possible the instrumental contributions to the peak broadening, and fulfilling a X-ray beam imprint smaller that the sample area. In order to quantitatively determine the amorphous volume fraction of the perturbed layer, a quantitative phase analysis was operated through the X-ray combined approach [15,16]. The measured crystalline phase corresponds to fluorapatite with various crystallite sizes and unit-cell dimensions (a and c) depending on the irradiation conditions (Table 2). The amorphous phase was modeled using the fluorapatite structure with elongated cell parameters and very small crystal sizes, typically from 40 Å to smaller than the crystal unit-cell. All the refinements were operated using the software package MAUD [17].

3. Results

The excitation curves (Fig. 1) exhibit two bumps after Kr ion irradiation at high fluence, like after Au ion irradiation [7]. The first one is always centered around a deuteron energy ($\sim$1.3 MeV) corresponding to the ^3He end-of-range (EOR) region (like the as-implanted sample excitation curve), called zone (1), and the second one corresponds to a zone closer to the surface, for lower deuteron

Table 1
Irradiation parameters for helium, krypton, iodine and gold ions: projected range (R_p), longitudinal straggling (ΔR_p), and electronic stopping power ($-dE/dx)_e$ at the incident energy (E) calculated with SRIM2010 code [11] (skeletal density: 2.838 g cm^{-3}).

Ion	$^3He^+$	$^{86}Kr^{21+}$	$^{127}I^{10+}$	$^{197}Au^{11+}$
E (MeV)	3	70	120	163
R_p (μm)	10.4	11.0	14.3	15.4
ΔR_p (μm)	0.23	0.46	0.59	0.74
$(-dE/dx)_e$ (keV nm^{-1})	0.21	10.9	15.1	20

Table 2
Amorphous fractions (F_a), unit-cell parameters (a and c), and cell volumes (V), deduced from the XRD data with the corresponding reliability factors (R_w, R_B) for the various ion irradiations (the 0 subscript denotes the virgin sample values, brackets are r.m.s. standard deviations obtained from the fit, on the last digit).

Fluence (cm^{-2})	F_a (%)	a (Å)	c (Å)	$\Delta a/a_0$ (%)	$\Delta c/c_0$ (%)	$\Delta V/V_0$ (%)	R_w (%)	R_B (%)
0	0	9.3365(3)	6.8560(5)	–	–	–	14.3	8.7
Kr								
10^{11}	0	–	–	–	–	–	–	–
10^{12}	0	–	–	–	–	–	–	–
5×10^{12}	51(1)	9.3775(9)	6.8912(8)	0.44(1)	0.51(1)	1.40(4)	24.2	15.1
10^{13}	80(1)	9.4236(5)	6.9105(5)	0.93(1)	0.79(1)	2.68(3)	9.9	6.0
5×10^{13}	86(1)	9.3160(4)	6.8402(5)	−0.22(1)	−0.23(1)	−0.67(3)	10.5	5.9
I								
5×10^{11}	14(2)	9.3603(3)	6.8790(5)	0.25(1)	0.34(1)	0.85(3)	23.9	15.1
3×10^{12}	53(2)	9.3645(3)	6.8840(5)	0.30(1)	0.41(1)	1.01(3)	13.3	9.0
5×10^{12}	71(5)	9.3765(5)	6.8881(6)	0.43(1)	0.47(2)	1.33(3)	10.4	7.3
10^{13}	87(2)	9.3719(4)	6.8857(6)	0.38(1)	0.43(2)	1.2(3)	6.7	4.9
Au								
2×10^{11}	27(8)	9.3530(1)	6.877(1)	0.18(1)	0.31(2)	0.66(5)	14.0	12.4
2.5×10^{11}	30(6)	9.3685(4)	6.8833(4)	0.34(1)	0.40(1)	1.09(3)	13.9	9.4
3×10^{11}	34(6)	9.3736(4)	6.8875(4)	0.40(1)	0.46(1)	1.26(3)	12.3	8.3
5×10^{11}	35(5)	9.3843(5)	6.8940(40)	0.51(1)	0.55(1)	1.59(3)	12.8	8.7
6×10^{11}	26(5)	9.3681(9)	6.8773(9)	0.34(1)	0.31(2)	0.99(5)	9.4	6.7
10^{12}	27(5)	9.3304(7)	6.8514(7)	−0.07(1)	−0.07(2)	−0.20(4)	13.8	9.6

energies, called zone (2). It is seen that the shape of the excitation curve depends on the fluence and ion species (Fig. 1). For Kr ion irradiation, at a fluence of 10^{12} cm^{-2}, the excitation curve actually flattens in an asymmetric way, thereby indicating that ^{3}He migrated towards the surface (Fig. 1a). At a larger fluence of 10^{13} cm^{-2}, the two bumps mentioned above are clearly seen. When increasing the electronic stopping power (Fig. 1b) for the same fluence (10^{12} cm^{-2}), the bump development is accentuated.

From XRD analysis, we have deduced the relative and absolute variations of the unit-cell parameters, for various fluences (Fig. 2 and Table 2). The evolution of the amorphous fraction (F_a) is also plotted as a function of fluence (Fig. 3). For the 163-MeV Au ion irradiation, the amorphous phase is detected at low fluence (F_a = 27% at 2×10^{11} cm^{-2}) (Table 2 and Fig. 3). This value is significantly larger than in our previous study with Kr and I ion irradiations [9]. For Kr ion irradiation, F_a is null up to a fluence of 5×10^{12} cm^{-2} and, for I ion irradiation, it is only equal to 14% for a fluence of 5×10^{11} cm^{-2} (Table 2 and Fig. 3) [9]. On the one hand, in the low-fluence range, F_a increases with the electronic stopping power. On the other hand, F_a increases up to a value about 35%, and exhibits a small decrease for Au ion irradiation, whereas it saturates at ~85–90% for I and Kr ion irradiations (Table 2 and Fig. 3) [9]. This increase of F_a is accompanied by an increase of unit-cell parameters and unit-cell volume of the crystalline phase (Fig. 2, Table 2) up to a fluence of 10^{13}, 5×10^{12} and 5×10^{11} cm^{-2} after Kr, I and Au ion irradiations respectively. This expansion of the unit-cell occurs equally along the two parameters. This seems consistent with the gradual increase of the cell volume previously observed on single crystals [9]. After this strong increase of the unit-cell with irradiation, for the highest fluences (up to 5×10^{13}, 10^{13} and 6×10^{11} cm^{-2} after Kr, I and Au ion irradiations respectively), the unit-cell parameters of the crystalline phase relax towards the pristine sample values (Table 2 and Fig. 2).

4. Data analysis

4.1. NRA data

The detected proton yield $I_0(E_0)$ at a given incident deuteron energy E_0 is considered as the convolution of the ^{3}He depth profile with the cross-section of the nuclear reaction ^{3}He(d, p)^{4}He [5,9,12,13]:

$$I_0(E_0) = \int_0^{x_0} \sigma(E(x))\rho(x)dx, \tag{1}$$

where x_0 is the deuteron projected range, σ is the cross-section, $E(x)$ is the deuteron energy at depth x (data given by the SRIM2010 code [11]), and $\rho(x)$ is the ^{3}He depth profile. The cross-section σ depends weakly on the angle of emission θ (for high angular values) at a given energy, [18] so that it is possible to neglect the angular dependence in Eq. (1). Moreover, we fixed a boundary condition for the distribution which must take a zero value at $x = 0$, because helium cannot accumulate at the surface.

To account for the existence of two accumulation zones, two diffusion equations are written. The first one relates to the accumulation zone (1) in the EOR region. In this zone, a part of ^{3}He atoms (with concentration ρ_1) could diffuse and be transported:

$$\frac{\partial \rho_1}{\partial t} = D_1 \frac{\partial^2 \rho_1}{\partial x^2} - v_1 \frac{\partial \rho_1}{\partial x} - g_{12} \cdot \rho_1, \tag{2}$$

where t is the irradiation time, D_1 is the diffusion coefficient, v_1 is the transport velocity and g_{12} is a detrapping coefficient from zone (1) to zone (2) that remains constant in time, until the maximum detrapped helium fraction ($1 - TP_1$) is reached, then becomes null. This condition on g_{12} means that a fraction of helium (TP_1) remains trapped probably on defects produced by elastic collisions in the EOR region. The coefficient TP_1 is equal to one if all helium atoms are trapped in the accumulation zone (1) and to zero if all atoms are detrapped.

Another part of ^{3}He atoms (with concentration ρ_2) coming from the initial as-implanted depth distribution (ρ_0) were shifted during the irradiation in the accumulation zone (2) where it could diffuse:

$$\frac{\partial \rho_2}{\partial t} = D_2 \frac{\partial^2 \rho_2}{\partial x^2} - v_2 \frac{\partial \rho_2}{\partial x} + g_{12} \cdot \rho_1 - F_2 \cdot \rho_2, \tag{3}$$

in which D_2 is the diffusion coefficient, and v_2 is the transport velocity. The coefficient F_2 corresponds to the volume of helium which was out-gassed from the sample. Applying this model thus consists of fitting seven free parameters (D_1, v_1, g_{12}, D_2, v_2, F_2 and TP_1) by using a trial-and-error method, based on the minimization of an error function between the experimental and calculated curves (Fig. 1). The quality of the fitted parameters is estimated by an error term, (noted as Err) displayed along with the optimized parameter values (Table 3). The ^{3}He depth profiles deduced from
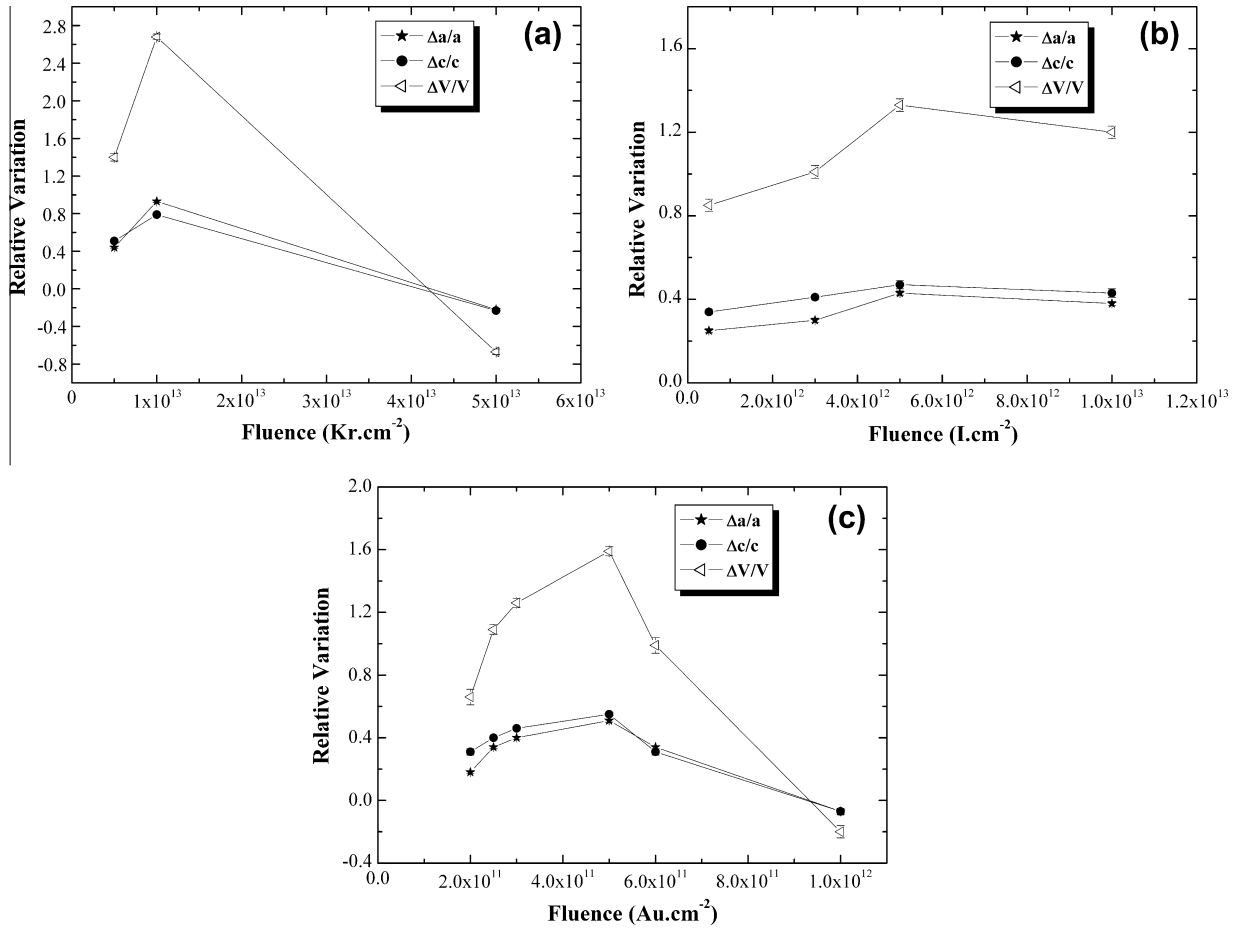
Fig. 2. Relative variations of unit-cell parameters (*a* and *c*) and cell volumes (*V*) for (a) Kr, (b) I and (c) Au ion irradiations.
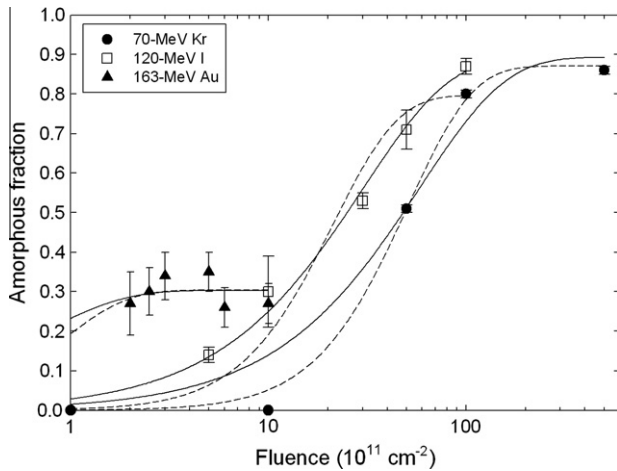

Fig. 3. Amorphous fractions deduced from XRD data versus fluence for the various ion irradiations. Lines are least-squares fits of the data to the (modified) single-impact model (Eq. (4), solid), and double-impact model (Eq. (5), dashed), respectively.

these optimizations are shown (Fig. 4). No assumptions were made on the shape of depth profiles except for the initial implantation profile $\rho_0(x)$ which was given a Gaussian shape in agreement with our previous results [6,12,13]. Finally, we have deduced (Table 4) the relative concentrations (ρ_1 and ρ_2) of both accumulation zones from these sets of optimized parameters.

4.2. XRD data

The amorphous fraction (F_a) data versus fluence ($\phi = \varphi t$) are often fitted with the single-impact model of damage used to model the kinetics of amorphization induced by ion track overlap (so-called Poisson's law) [19]. We previously applied [9,10] a modified single-impact model, with a saturation value (F_{sat}) lower than 100%, which fits I ion data well (Fig. 3):

$$F_a = F_{sat}(1 - e^{-A\phi}), \tag{4}$$

where A is a damage cross-section.

In the case of Kr ion data (Fig. 3), the best fit is obtained with a modified double-impact model, also with a saturation value (F_{sat}) lower than 100%, considering that *at least* two impacts are needed to produce the amorphous phase [20]:

$$F_a = F_{sat}[1 - (1 + A\phi)e^{-A\phi}]. \tag{5}$$

The saturation amorphous fraction (F_{sat}) clearly decreases, and the cross-sections increase (for both damage models), with electronic stopping power from Kr to Au ions (Table 5).

However, the application of such simple approaches to the present case with saturation values lower than 100% is not fully justified. There must be at least one effect competing with the amorphization process to account for the limits of saturation values.

In the case of the single-impact model, the rate equation may be written as:

$$dF_a/d\phi = A'(1 - F_a) - SF_a, \tag{6}$$

Table 3
Optimized ³He profile parameters with the corresponding errors (Err) obtained by the AGEING computer code for the three different irradiation conditions (see text for the symbols).

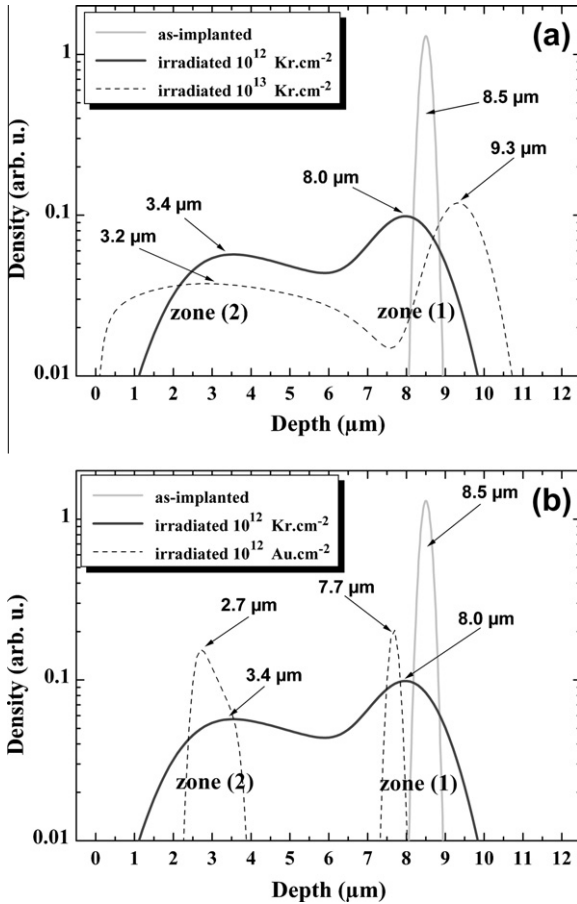| Ion	Fluence (cm⁻²)	D_1 (cm² s⁻¹)	v_1 (cm s⁻¹)	TP_1 (%)	g_{12} (s⁻¹)	D_2 (cm² s⁻¹)	v_2 (cm s⁻¹)	F_2 (%)	Err (%)
Kr	10^{12}	1.37×10^{-11}	6.96×10^{-8}	0.33	1.17×10^{-2}	5.55×10^{-11}	4.55×10^{-7}	0	3.33
Kr	10^{13}	3.18×10^{-12}	-7.5×10^{-9}	0.30	1.08×10^{-4}	1.17×10^{-11}	7.90×10^{-8}	8	3.84
Au	10^{12}	3.09×10^{-16}	7.51×10^{-8}	0.18	6.97×10^{-3}	2.65×10^{-16}	5.48×10^{-7}	54	2.23

Fig. 4. ³He depth profiles obtained with the AGEING computer code: at different fluences for Kr ion irradiation (a), and different electronic stopping powers for Kr and Au ion irradiations at the same fluence (10^{12} cm⁻²) (b).

Table 4
Optimized ³He profile parameters obtained by the AGEING computer code for the three different irradiation conditions: relative concentrations in zone (1) (ρ_1) and zone (2) (ρ_2), and helium loss term (F_2).

Ion	Fluence (cm⁻²)	ρ_1 (%)	ρ_2 (%)	F_2 (%)
Kr	10^{12}	36	64	0
Kr	10^{13}	30	62	8
Au	10^{12}	16	30	54

where A' is a damage cross-section and S a recovery cross-section inside the ion tracks. For $S = 0$, integration of Eq. (6) gives the standard single-impact model of Eq. (4) with $F_{sat} = 100\%$ [19]. For $S \neq 0$, the solution is given by:

$$F_a = [A'/(A' + S)][1 - e^{-(A'+S)\phi}],\qquad(7)$$

that is equivalent to Eq. (4) with a saturation value $F_{sat} = A'/(A' + S)$, and a cross-section $(A' + S) = A'/F_{sat}$ instead of A. It means that the cross-sections deduced from these plots are overestimated,

Table 5
Amorphization cross-sections (A and $A' = A F_{sat}$), recovery cross-section (S), effective track-core radius ($R_e = (A/\pi)^{1/2}$ and $R'_e = (A'/\pi)^{1/2}$), saturation values of amorphous fractions (F_{sat}) deduced from XRD data for the three ion irradiations with Eqs. (4), (5), and (7), and reliability factor of least-squares fits (χ).

	Kr	I	Au
Single-impact model Eqs. (4) and (7)			
A (10^{-13} cm²)	1.7 ± 0.4	3.3 ± 0.4	146 ± 124
R_e (nm)	2.3 ± 0.3	3.2 ± 0.2	22 ± 9.3
A' (10^{-13} cm²)	1.5 ± 0.6	3.0 ± 0.5	43.8 ± 40.1
S (10^{-13} cm²)	0.2 ± 1.1	0.3 ± 0.1	102.2 ± 100.3
R'_e (nm)	2.2 ± 0.4	3.1 ± 0.3	12 ± 5.5
F_{sat} (%)	87 ± 9	90 ± 4	30 ± 2
χ	0.025	0.003	0.007
Double-impact model Eq. (5)			
A (10^{-13} cm²)	3.9 ± 0.3	9.5 ± 1.9	217 ± 119
F_{sat} (%)	85 ± 3	80 ± 7	30 ± 2
χ	0.003	0.032	0.007

especially in the case of Au ion data. Cross-sections deduced from fits (Table 5) are thus $(A' + S) = A'/F_{sat}$ instead of A by using the modified single-impact model of Eq. (4), thus $A' = (A' + S) F_{sat} = A F_{sat}$, and $S = A' (1/F_{sat} - 1)$. Assuming that A' is the amorphous track cross-section, one has $A' = \pi R'^2_e$, where R'_e is the effective track-core radius (Table 5). The latter R'_e values are smaller than the previous R_e values deduced from uncorrected A-values (with $A = \pi R^2_e$) [9,10].

5. Discussion

5.1. Damage evolution

XRD data shows that at low fluence, the amorphous fraction (F_a) increases with the electronic stopping power (Table 2 and Fig. 3). The same behavior is found for the amorphization cross-section (Table 5), the unit-cell parameters, and unit-cell volume (Table 2). It is seen that F_a saturates at ∼85–90% for Kr and I ions and ∼35% for Au ions (Table 2). This saturation value is a good indication that another process competes with the amorphization process, i.e. a recrystallization process. This recrystallization effect is stronger for Au ions than for Kr and I ions: we assume that it increases with the electronic stopping power. The fact that a complete amorphization of fluorapatite cannot be obtained even for high fluences, confirms the defect-healing behavior of this material already observed upon α-particle irradiation, [21] and shows the existence of a defect-healing process for high electronic stopping power. This recrystallization is accompanied by stress relaxation (Table 2 and Fig. 2). After a strong increase to the unit-cell with irradiation, for the highest fluences, the unit-cell parameters of the crystalline phase are shifting back to the values prior to irradiation. The elastic strain of the crystalline phase is almost fully relaxed.

The reliability factor χ (Table 5) shows that the double-impact model is the most appropriate for Kr ion irradiation, whereas the single-impact model is the best one for I ion irradiation. A single I ion impact allows the creation of an amorphous core in latent tracks, whereas a double Kr ion impact is necessary to amorphize

the fluorapatite, the first impact giving rise to small "pre-damaged" domains. The effective radius of amorphization (R'_e) for both models increases with the electronic stopping power (Table 5). This confirms that amorphization is enhanced at low fluences with increasing electronic stopping power.

For Kr ion irradiation, direct TEM observation of incompletely amorphized tracks corresponding to a single impact gave a radius of 2.05 nm, [9] in rather good agreement with the single-impact model analysis ($R'_e = 2.2$ nm) (Table 5). For Kr and I ion irradiations, the effective radius R'_e is slightly smaller than R_e, in agreement with the low value of the recovery cross-section S. In both cases, Eq. (4) is sufficient to give a good approximation of the effective radius.

For Au ion irradiation, the new data analysis (Eq. (7)) gives lower amorphization cross-sections A' and effective track-core radii R'_e than the modified single impact model (Eq. (4)), in agreement with the important value of the recovery cross-section S (Table 5). However, owing to the lack of low-fluence data below the saturation, these cross-section values are still not very accurate, and certainly overestimated. There is no clear difference between least-squares fits using the single and double impact models.

5.2. Helium diffusion

Previous studies have shown that NRA is well suited to determine the evolution of implanted ^{3}He depth profiles upon thermal annealing [5,6,12,13]. In the present results, it is seen that the optimized curves reproduce well the shapes of excitation curves (Fig. 1a and b) with an error term (Err) less than 4% (Table 3). The excitation curves in the case of Kr ion irradiation exhibit two bumps (Fig. 1) corresponding to different depths of the ^{3}He profiles (Fig. 4), like in the case of Au ion irradiation (Figs. 1b–4b) [7]. The first maximum is located at a depth of 8.0 and 9.3 μm for samples irradiated with Kr ions for fluences of 10^{12} and 10^{13} cm^{-2} respectively (Fig. 4a), and 7.7 μm, for a fluence of 10^{12} cm^{-2} with Au ions (Fig. 4b). These depths are quite close to those determined on the as-implanted samples (8.5 μm) (Fig. 4).

The second maximum is closer to the surface at depths of 3.4 and 3.2 μm for samples irradiated with Kr ions for fluences of 10^{12} and 10^{13} cm^{-2} respectively (Fig. 4a), and at 2.7 μm for a fluence of 10^{12} cm^{-2} with Au ions (Fig. 4b). Hence, ^{3}He tends to accumulate at depths half way between the surface and the first maximum. The second accumulation zone seems to arise from helium transport to the surface induced by irradiation.

The optimized parameters values (Table 3) allow some general qualitative remarks on the observed trends. It is seen that the fraction of helium ($1 - TP_1$) which was detrapped from zone (1), and the loss term (F_2) are clearly increased for a larger electronic stopping power at the same ion fluence (10^{12} cm^{-2}). The ^{3}He diffusion coefficients in zone (1) (D_1) and zone (2) (D_2) are about the same for a given ion irradiation. However, they both decrease with fluence and stopping power. This is consistent with a trapping increasing with ion damage.

SRIM2010 simulations show that the maximum displacement per atom reached with the heavy ion irradiations is about one order-of-magnitude smaller than with ^{3}He ion implantation. The trapping of helium atoms by defects induced by nuclear collisions in the EOR region (corresponding to zone (1)) is thus quite inefficient, in contrast to the case of ^{3}He induced by 220-MeV proton irradiations for which helium diffusion was clearly impeded [22]. We thus assume that this effect is caused by the electronic stopping power in this material which is shown to be sensitive to electronic excitations on the basis of the XRD data (Fig. 3). Indeed, this effect is consistent with the enhancement of the recrystallization effect with increasing electronic stopping power from 70-MeV Kr and 120-MeV I ions to 163-MeV Au ions (Fig. 3), as discussed

above. This supports our interpretation of a RED effect in relation to the damage induced by electronic excitations [7].

By contrast, the transport velocity (v_2) in zone (2) is about one order-of-magnitude larger than in zone (1) (v_1) for both Kr and Au ion irradiations (Table 3). This is consistent with the large fraction of helium gas ($TP_1 \sim 20$–30%) that remained trapped in zone (1), which decreases with stopping power for the same fluence (10^{12} cm^{-2}), as already mentioned above.

This is also in agreement with the significant part of ^{3}He (corresponding to the coefficient g_{12}) that was shifted to zone (2) upon irradiation. A similar value ($g_{12} \sim 10^{-2}$ s^{-1}) is found for both ion species at the same fluence (10^{12} cm^{-2}), which decreases by two orders of magnitude with fluence for Kr ions (Table 3). This shows that, once helium atoms have been shifted from zone (1) to zone (2), they are more strongly trapped in the latter zone with little effect of subsequent ion impacts. We assume that the ion-induced recrystallization process generates diffusion barriers which impedes further shift of the helium depth profile to the surface [7]. This second peak in the depth profiles cannot be attributed to a sputtering effect at such large depths.

The loss term (F_2) is equal to zero only in the case of Kr ion irradiation at the lowest fluence (10^{12} cm^{-2}) (Table 3). This loss is seen to increase with fluence (for Kr ions) and electronic stopping power ($F_2 = 54\%$ for Au ions). This indicates that a significant part of helium gas has escaped from the solid. This feature is consistent with the cracks that were previously observed with Au ion irradiation, [7] and the blistering and exfoliation in fluorapatite single crystals upon ^{4}He ion implantation [21]. As mentioned previously, [7] this is certainly enhanced with the high stopping power of swift heavy ions, even for a ^{3}He peak concentration (~ 0.3 at.%) much lower than the critical concentration (5 at.%) for exfoliation [21].

6. Conclusions

Fluorapatite (Ca$_{10}$(PO$_4$)$_6$F$_2$) sinters were irradiated by swift heavy ions with energies ~ 0.8–0.9 MeV amu^{-1} in the electronic slowing down regime. At low fluences, the amorphous fractions deduced from the powder XRD data increase with the electronic stopping power for a given fluence. This is accompanied by an expansion of the unit-cell parameters. Yet, at high fluences, the damaged fraction saturates at ~ 85–90% for Kr and I ion irradiations and only at 35% for Au ion irradiation. This in-beam damage healing increases with electronic stopping power and is accompanied by a relaxation of the unit-cell parameters. This damage healing is assigned to an ion-induced recrystallization process which puts a limit to the damaged fraction. A significant ion-induced He diffusion to the sample surface is found by non-destructive NRA with a characteristic two-bump depth distribution at high fluences. Part of implanted ^{3}He atoms were trapped in the end-of-range region, whereas a significant helium fraction migrated towards the surface upon irradiation and was trapped below the surface. A strong He gas release effect is also deduced from the NRA data. This helium loss increases with fluence and electronic stopping power up to 54% for Au ion irradiation. All these data are interpreted by a RED effect increasing with fluence and electronic stopping power.

References

[1] C. Rey, L'actualité Chimique 7 (1995) 41.
[2] W.J. Weber et al., J. Mater. Res. 13 (1998) 1434.
[3] D.J. Reed, Radiat. Eff. 31 (1977) 129.

[4] S.E. Donnelly, J.H. Evans (Eds.), Fundamentals of Inert Gases in Solids, Plenum, New York, 1991.

[5] D.J. Cherniak, E.B. Watson, J.B. Thomas, Chem. Geol. 268 (2009) 155.

[6] S. Miro, F. Studer, J.M. Costantini, J. Haussy, P. Trouslard, J.J. Grob, J. Nucl. Mater. 355 (2006) 1.

[7] S. Miro, F. Studer, J.M. Costantini, P. Berger, J. Haussy, P. Trouslard, J.J. Grob, J. Nucl. Mater. 362 (2007) 445.

[8] S. Miro, PhD Dissertation, Caen University, 2003.

[9] S. Miro, D. Grébille, D. Chateigner, D. Pelloquin, J.P. Stoquert, J.J. Grob, J.M. Costantini, F. Studer, Nucl. Instrum. Meth. B 227 (2005) 306.

[10] S. Miro, J.M. Costantini, J.-F. Bardeau, D. Chateigner, F. Studer, F. Balanzat, J. Raman Spectrosc. doi:10.1002/jrs.2955.

[11] J.F. Ziegler, J.P. Biersack, U. Littmark, The Stopping and Ranges of Ions in Solids, vol. 1, Pergamon, New York, 1985. http://www.srim.org/.

[12] J.M. Costantini, P. Trocelier, J. Haussy, J.J. Grob, Nucl. Instr. Meth. B 195 (2002) 400.

[13] J.M. Costantini, J.J. Grob, J. Haussy, P. Trocellier, P. Trouslard, J. Nucl. Mater. 321 (2003) 281.

[14] J. Ricote, D. Chateigner, L. Pardo, M. Algueró, J. Mendiola, M.L. Calzada, Ferroelectrics 241 (2000) 167.

[15] D. Chateigner, L. Lutterotti, T. Hansen, ILL Highlights 97 (1998) 28.

[16] D. Chateigner (Ed.), Combined Analysis, Wiley-ISTE, 2010, p. 496p (ISBN: 978-1-84821-198-8).

[17] L. Lutterotti, S. Matthies, H.R. Wenk, in: J.A. Szpunar (Ed.), Textures of Materials, vol. 2, NRC Research Press, Ottawa, 1999. p. 1599.

[18] J.R. Tesmer, M. Nastasi (Eds.), Handbook of Modern Ion-Beam Materials Analysis, MRS, Pittsburgh, 1995. p. 159.

[19] R. Spohr, Ion Tracks and Microtechnology, Vieweg, Braunscshweig, 1990.

[20] C. Gibert-Mougel, F. Couvreur, J.M. Costantini, S. Bouffard, F. Levesque, S. Hémon, E. Paumier, C. Dufour, J. Nucl. Mater. 295 (2001) 121.

[21] S. Soulet, J. Carpéna, J. Chaumont, O. Kaitasov, M.O. Ruault, J.C. Krupa, Nucl. Instr. Meth. B 184 (2001) 383.

[22] D.L. Shuster, R.M. Flowers, K.A. Farley, Earth Planet. Sci. Lett. 249 (2006) 148.